remote sensing

MDPI

Supplementary Material

Contents of this file

Figures S1 to S10
Table S1

Introduction

This supporting information includes:

1) Supplementary Figure for roughness computation approach.
2) Supplementary Figure for Gaussian Kernel Regression for HM_05
3) Supplementary Figure for Gaussian Kernel Regression for HM_12
4) Supplementary Figure for Gaussian Kernel Regression for HM_32
5) Supplementary Figure showing 'MSH_TEST' study area backscatter maps.
6) Supplementary Figures of the 'MSH_01' study area backscatter maps.
7) Supplementary Figure showing 'MSH_TEST' study areas surface roughness maps.
8) Supplementary Figure of binary wet snow maps.
9) Supplementary Figure of snow extent in 'MSH_01' study area.
10) Supplementary Table of ASAR-ISRO Image Noise Bias values applied in computation of backscatter and surface roughness over Mount St. Helens (WA) region.

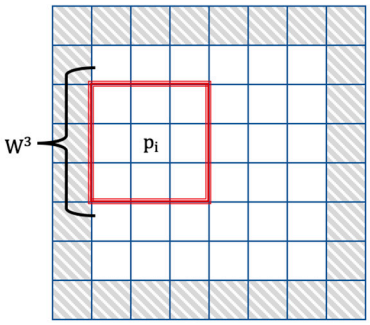

Figure S1. Roughness Computation with a 3 x 3 Window. To compute the roughness of a pixel of interest, p_i, in an 8 x 8 input image, a 3 x 3 window, W^3, is placed with its center on p_i and the corresponding roughness is computed as the mean absolute deviation of the set of pixels contained within the window. The roughness is not computed for border pixels (shaded) that are unable to accommodate a complete window.

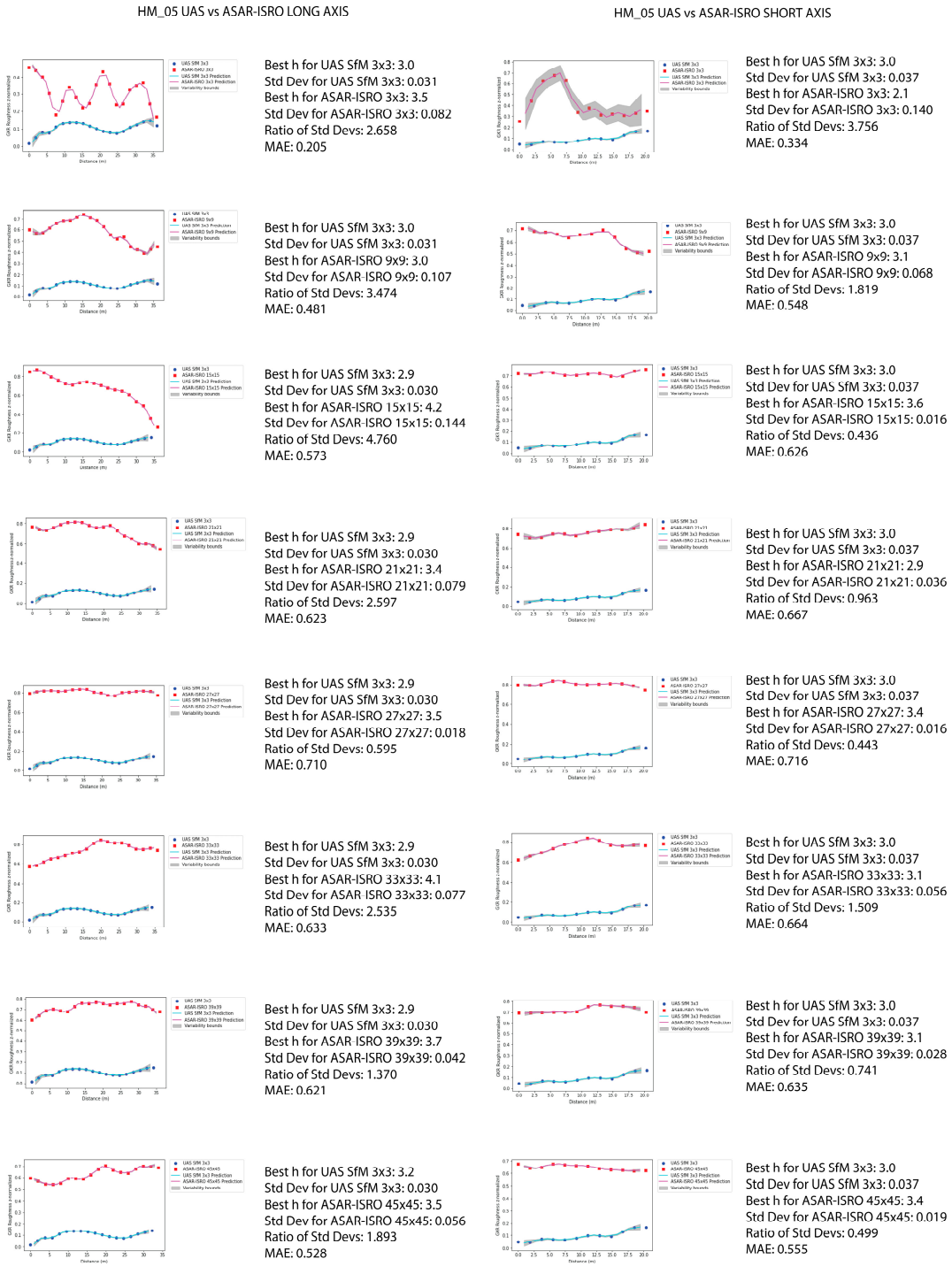

Figure S2. Gaussian kernel regression (GKR) plots for HM_05. Plots show Gaussian kernel regression trendlines for 3 x 3 UAS SfM derived roughness versus the ASAR-ISRO derived roughnesses from 3 x 3 to 45 x 45 (in 3 x 3 increments) on each, the long axis (left column) and short axis (right column) of the selected hummock HM_05. The bandwidth parameter *h* was calibrated using a K-Fold cross-validation approach to find the best bandwith value for each platform in each window comparison iteration for the kernel regression. Variability bounds indicate a 95% confidence interval on the predicted GKR trendlines.

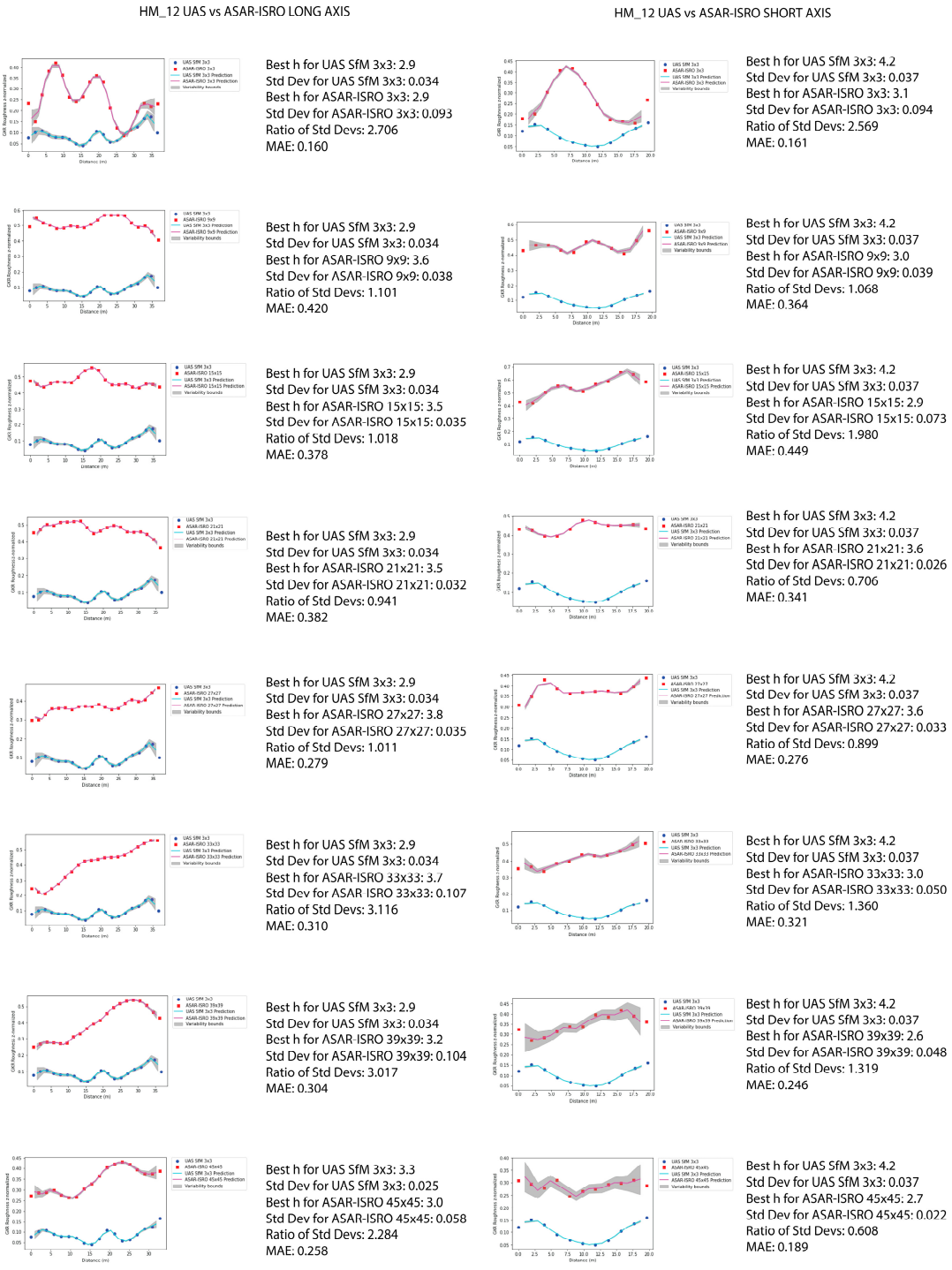

Figure S3. Gaussian kernel regression (GKR) plots for HM_12. Plots show Gaussian kernel regression trendlines for 3 x 3 UAS SfM derived roughness versus the ASAR-ISRO derived roughnesses from 3 x 3 to 45 x 45 (in 3 x 3 increments) on each, the long axis (left column) and short axis (right column) of the selected hummock HM_12. The bandwidth parameter *h* was calibrated using a K-Fold cross-validation approach to find the best bandwith value for each platform in each window comparison iteration for the kernel regression. Variability bounds indicate a 95% confidence interval on the predicted GKR trendlines.

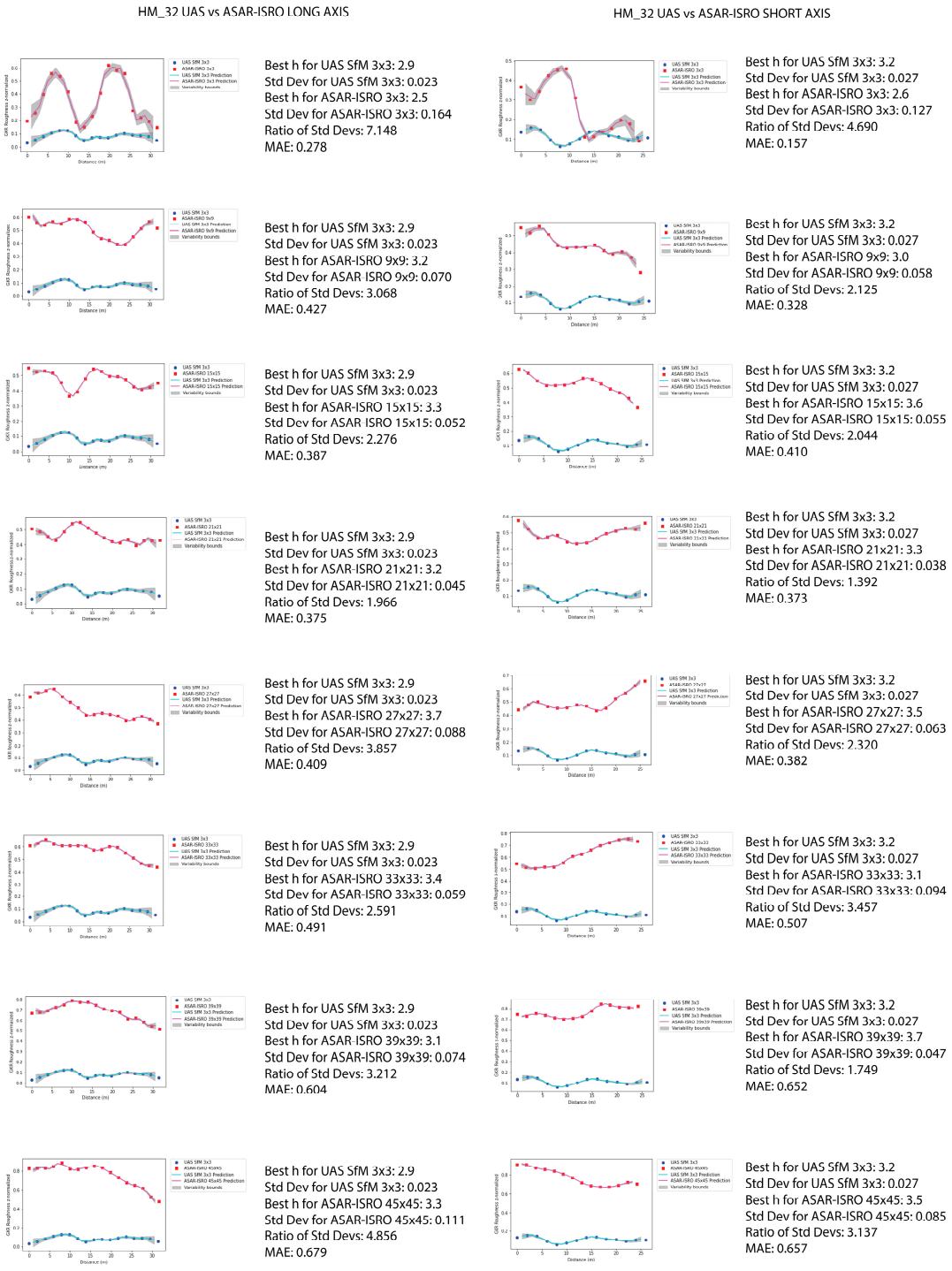

Figure S4. Gaussian kernel regression (GKR) plots for HM_32. Plots show Gaussian kernel regression trendlines for 3 x 3 UAS SfM derived roughness versus the ASAR-ISRO derived roughnesses from 3 x 3 to 45 x 45 (in 3 x 3 increments) on each, the long axis (left column) and short axis (right column) of the selected hummock HM_32. The bandwidth parameter *h* was calibrated using a K-Fold cross-validation approach to find the best bandwith value for each platform in each window comparison iteration for the kernel regression. Variability bounds indicate a 95% confidence interval on the predicted GKR trendlines.

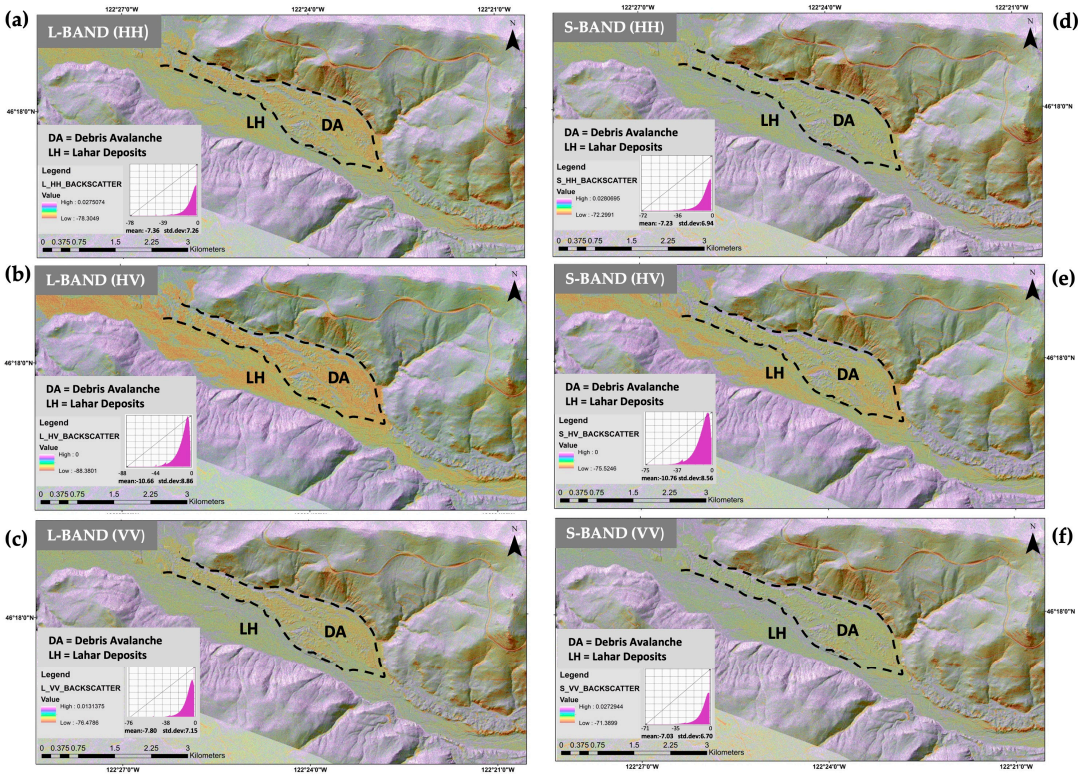

Figure S5. 'MSH_TEST' study area backscattering maps in (**a–c**) L-band and (**d–f**) S-band, showing a measurable backscatter variation for each band and individual polarization. For visual clarity, ASAR-ISRO backscattering data were superimposed on a 3-m LiDAR DEM of Mount St. Helens [39].

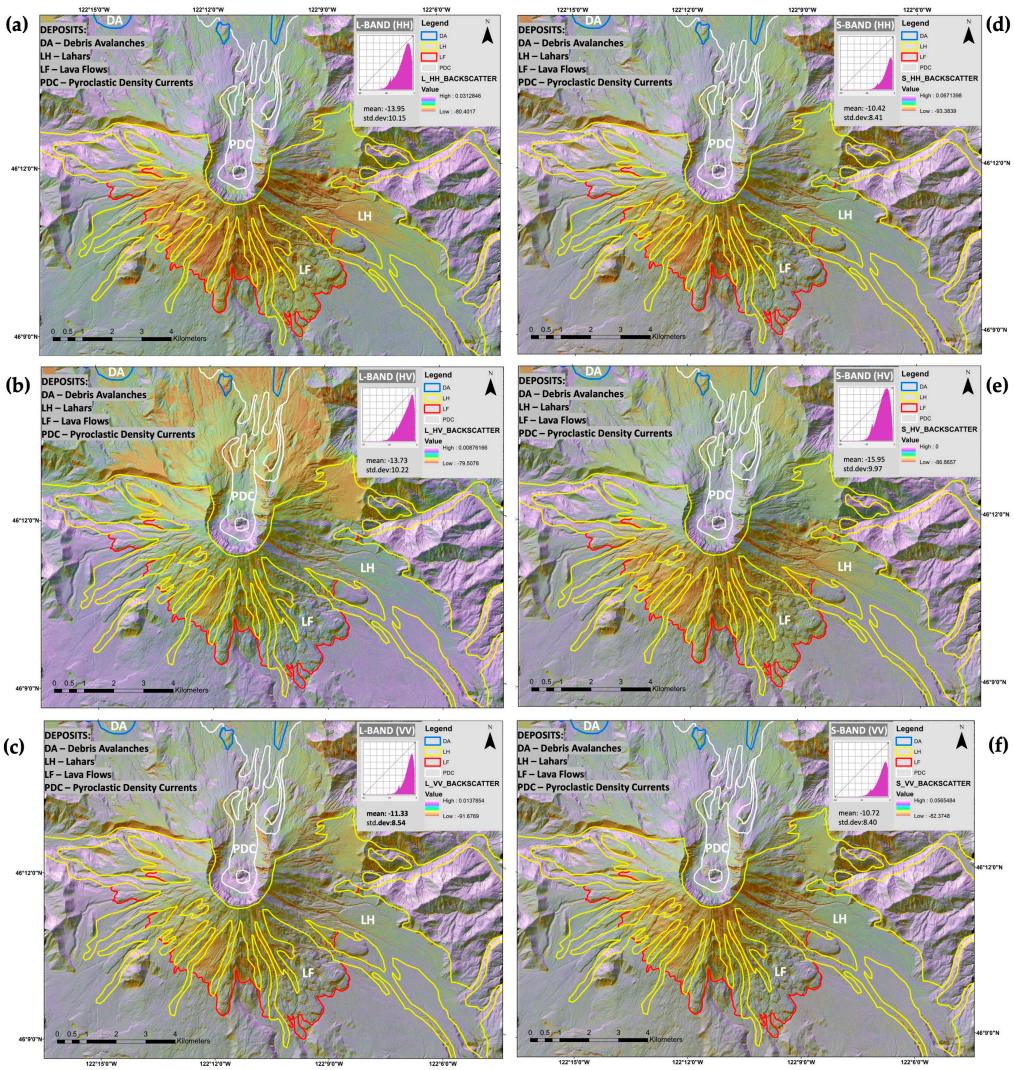

Figure S6. 'MSH_01' study area backscattering maps, showing a measurable backscatter variation between (**a–c**) L-band and (**d–f**) S-band, and individual polarization (HH, HV & VV). For visual clarity, ASAR-ISRO backscattering data were superimposed on a 3-m LiDAR DEM of Mount St Helens [36]. The extent of LH, LF, PDC and DA deposits (extracted from [34,40]) are superimposed on backscattering results and are indicated in yellow, red, white and blue respectively.

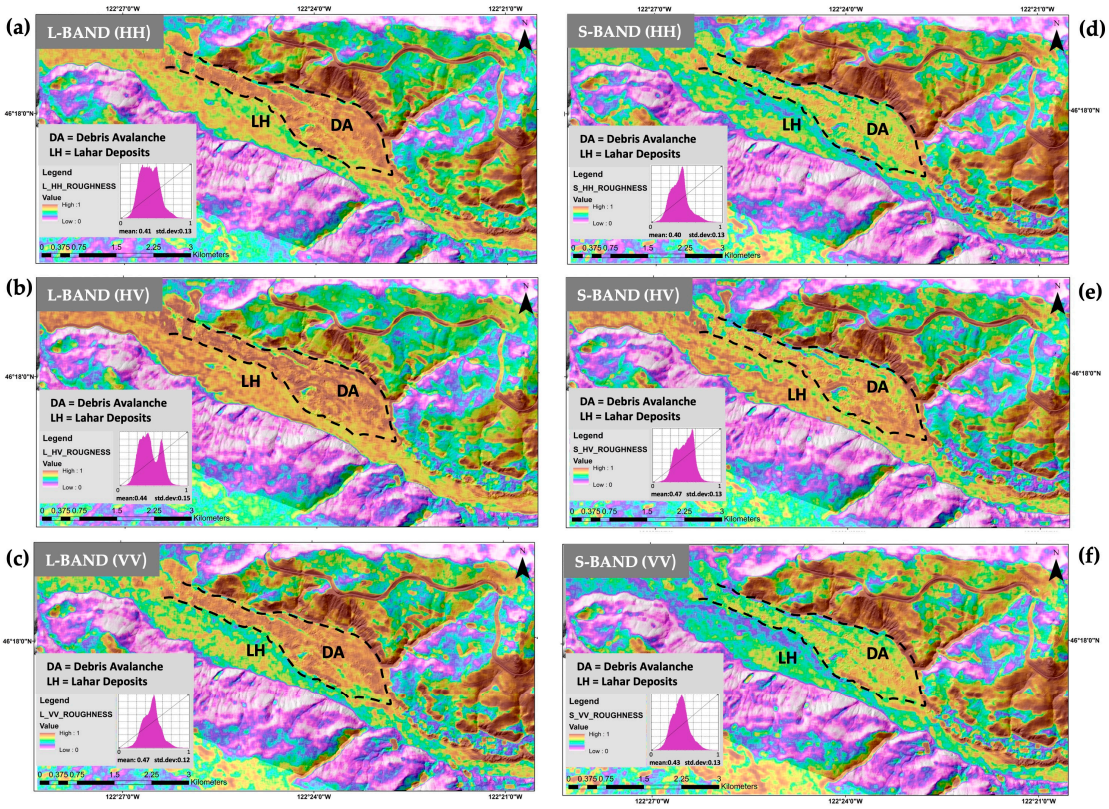

Figure S7. Surface roughness maps for 'MSH_TEST', derived from ASAR-ISRO backscatter data, using *Equation 7* with a 41 × 41 window, superimposed on a 3-m LiDAR DEM of Mount St. Helens [39], where (**a–c**) is the L-band and (**d–f**) is the S-band, shown in co-polarized (HH and VV) and cross-polarized (HV) modes.

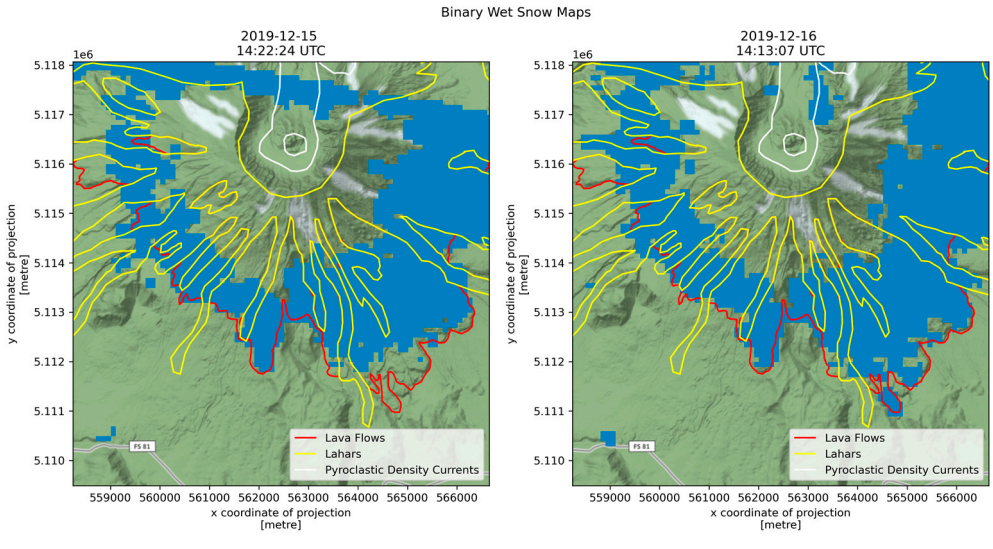

Figure S8. Binary wet snow maps produced using Sentinel-1 acquisitions on **(a)** 15 December 2019 and **(b)** 16 December 2019. Blue pixels represent wet snow. For 15 December 2019 acquisition, note the Sentinel-1 scene boundary on the north-side running diagonally down from left to right with some possible false-positive wet snow signals, as well as missing values outside the scene.

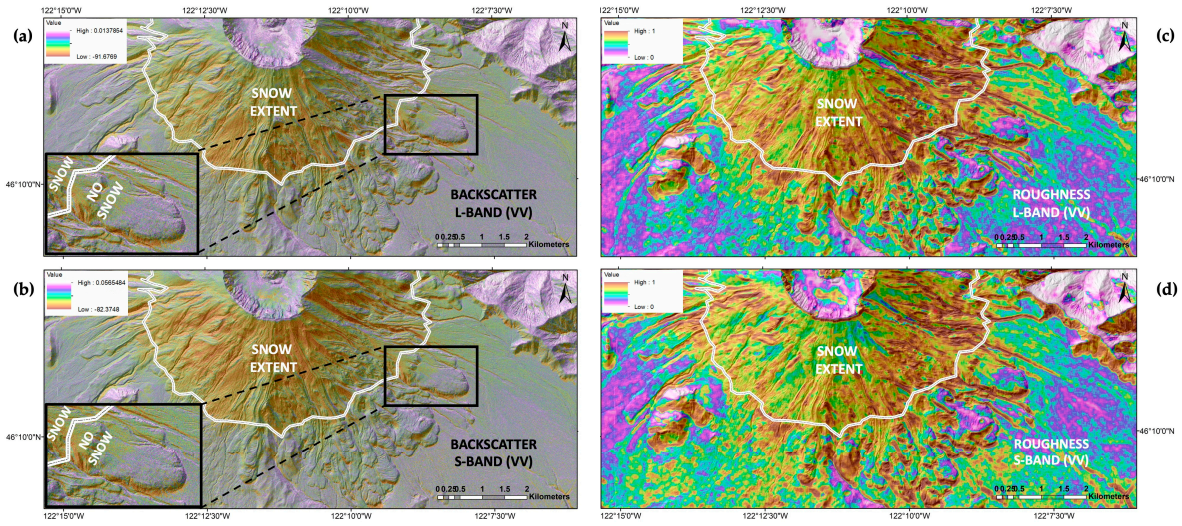

Figure S9. Snow extent (white outline) for the 'MSH_01' study area, indicating its effect on (a) backscatter and (b) surface roughness results. Backscatter and surface roughness data are superimposed on a 3-m LiDAR DEM of Mount St. Helens [39].

Strip	Band	Image Noise Bias (*N*) at Different Polarization Modes			
		HH	**HV**	**VH**	**VV**
27124	**L**	1.762430	1.232394	1.891561	1.325989
	S	28.939447	18.862608	22.566810	26.170986
27126	**L**	1.324492	1.353610	1.421536	1.456411
	S	27.497353	19.322093	21.447556	26.815105
27127	**L**	0.655546	0.645208	0.703577	0.694209
	S	14.859436	11.114200	11.399114	15.169984
27128	**L**	0.6611792	0.6476600	0.710281	0.696782
	S	16.934081	12.436480	12.830074	16.764993

Table S1. Image Noise Bias Values. The image noise bias associated with each level-2 product dataset. When used along with the corresponding digital number, per-pixel incidence angle, and calibration constant, the backscattering coefficient may be computed (*Equation* 2).